LETTER

doi:10.1038/nature10577

Atomic–resolution dynamics on the surface of amyloid–β protofibrils probed by solution NMR

Nicolas L. Fawzi[1], Jinfa Ying[1], Rodolfo Ghirlando[2], Dennis A. Torchia[3] & G. Marius Clore[1]

Exchange dynamics between molecules free in solution and bound to the surface of a large supramolecular structure, a polymer, a membrane or solid support are important in many phenomena in biology and materials science. Here we present a novel and generally applicable solution NMR technique, known as dark-state exchange saturation transfer (DEST), to probe such exchange phenomena with atomic resolution. This is illustrated by the exchange reaction between amyloid-β (Aβ) monomers and polydisperse, NMR-invisible ('dark') protofibrils, a process of significant interest because the accumulation of toxic, aggregated forms of Aβ, from small oligomers to very large assemblies, has been implicated in the aetiology of Alzheimer's disease[1–6]. The ^{15}N-DEST experiment imprints with single-residue-resolution dynamic information on the protofibril-bound species in the form of ^{15}N transverse relaxation rates (^{15}N-R_2) and exchange kinetics between monomers and protofibrils onto the easily observed two-dimensional ^{1}H–^{15}N correlation spectrum of the monomer. The exchanging species on the protofibril surface comprise an ensemble of sparsely populated states where each residue is either tethered to (through other residues) or in direct contact with the surface. The first eight residues exist predominantly in a mobile tethered state, whereas the largely hydrophobic central region and part of the carboxy (C)-terminal hydrophobic region are in direct contact with the protofibril surface for a significant proportion of the time. The C-terminal residues of both Aβ40 and Aβ42 display lower affinity for the protofibril surface, indicating that they are likely to be surface exposed rather than buried as in structures of Aβ fibrils[7–10], and might therefore comprise the critical nucleus for fibril formation[11,12]. The ^{15}N$-R_2^{tethered}$ values, however, are significantly larger for the C-terminal residues of Aβ42 than Aβ40, which might explain the former's higher propensity for rapid aggregation and fibril formation[13,14].

We recently reported the existence of a dynamic exchange process under pseudo-equilibrium conditions between monomeric and very high molecular mass, soluble species of Aβ40 (ref. 15). The latter form spontaneously in concentrated (150–300 μM) unstirred aqueous solution, and comprise polydisperse, non-fibrillar aggregates typical of worm-like protofibrils (Supplementary Fig. 1a). Similar protofibrils are formed by Aβ42 under the same conditions (Supplementary Fig. 1b). These protofibrils, which we have characterized extensively by atomic force and electron microscopy (Supplementary Fig. 1), analytical ultracentrifugation (Supplementary Fig. 3) and dynamic light scattering (Supplementary Fig. 4) are far too large (1.8–85 MDa) to detect directly using solution NMR spectroscopy as their resonances are broadened beyond detection[15], and their heterogeneous nature makes biophysical characterization challenging[5,16–19]. Both the Aβ40 and Aβ42 protofibrils present in the equilibrated concentrated samples react strongly with the OC polyclonal antibody that recognizes so-called 'fibrillar' oligomers and fibrils[3] (Supplementary Fig. 6b); the A11 polyclonal antibody recognizes so-called 'pre-fibrillar' oligomers[3] and reacts with both Aβ40 and Aβ42 protofibrils, albeit weakly with the former (Supplementary Fig. 6a). The predominantly unstructured, intrinsically disordered, monomeric Aβ peptides[20,21], however, give rise to excellent solution NMR spectra[15] (Supplementary Fig. 7), and analytical ultracentrifugation indicates unambiguously that the NMR visible species is monomeric, and that there are no measurable quantities of low molecular mass oligomers present in either the dilute (Supplementary Fig. 2) or concentrated (Supplementary Fig. 5) samples. Indeed, in the concentrated samples containing monomer and protofibrils, there is no evidence by analytical ultracentrifugation of any species other than monomer and protofibrils with M_r in excess of 1.8 MDa (Supplementary Figs 4 and 5). In this work, we probe the protofibril-bound species at a residue-by-residue level using ^{15}N-DEST, a novel two-dimensional transfer-of-saturation NMR experiment that exploits the exchange process between NMR invisible ('dark state') and easily observed monomeric states.

The essence of the two-dimensional ^{15}N-DEST experiment is based on the dramatic reduction in rates of re-orientation upon binding to the surface of the protofibrils resulting in transverse relaxation rates (^{15}N-R_2) that are orders of magnitude larger than those of the free monomer. These large ^{15}N-R_2 values preclude direct observation by solution NMR, but allow for efficient partial saturation of ^{15}N longitudinal magnetization of the protofibril-bound form by a weak radio-frequency field, even at large offsets where the free monomer magnetization is completely unaffected. In the DEST experiment, ^{15}N longitudinal magnetization of the free monomer is prepared (INEPT and refocused INEPT transfer), transferred by chemical exchange to the protofibril-bound form (binding), partly saturated (weak ^{15}N saturation at a series of offsets) and transferred back to the free monomer (dissociation) where the partial saturation is recorded as an attenuation of the cross-peaks of the NMR observable free monomer relative to that in a reference spectrum obtained without saturation (see Methods and Supplementary Fig. 8).

NMR measurements were made at 10 °C, pH 6.8 using two concentrations of Aβ: a low concentration sample (50 μM) at which both Aβ40 and Aβ42 remain nearly entirely monomeric (>90%) for a long period of time (>2 months for Aβ40 and approximately 1 week for Aβ42) based on cross-peak intensities in a ^{1}H–^{15}N heteronuclear single quantum coherence correlation spectrum; and a higher concentration sample in which the fraction of monomer decreases rapidly (over approximately 2 days for Aβ42 and 1 week for Aβ40) after which a stable pseudo-equilibrium between monomer and protofibrils is maintained for more than a week[15] (Supplementary Fig. 9). The amount of protofibrils formed at a given initial concentration of Aβ is significantly higher for Aβ42 than Aβ40 (Supplementary Fig. 9). Thus, for 270 μM Aβ40 and 160 μM Aβ42 samples, the concentration of monomer decreases to pseudo-steady-state levels of approximately 110 and 35 μM, respectively.

For the monomeric Aβ40 sample, the ^{1}H–^{15}N cross-peaks in the DEST experiment display an extremely sharp saturation profile with

[1]Laboratory of Chemical Physics, National Institute of Diabetes and Digestive and Kidney Diseases, National Institutes of Health, Bethesda, Maryland 20892-0520, USA. [2]Laboratory of Molecular Biology, National Institute of Diabetes and Digestive and Kidney Diseases, National Institutes of Health, Bethesda, Maryland 20892-0520, USA. [3]National Institute of Dental and Craniofacial Research, National Institutes of Health, Bethesda, Maryland 20892-0520, USA.

no detectable attenuation for any residue until the saturation pulse is less than 2 kHz from the ^{15}N resonance frequencies of the monomer (Fig. 1a, circles). This behaviour, replicated for the monomeric Aβ42 sample, matches the predicted saturation profile for a ^{15}N spin with relaxation parameters measured for the monomeric species (Fig. 1a, solid line). In contrast, the ^{1}H–^{15}N cross-peaks in the 270-μM Aβ40 sample show significant partial saturation at offsets far from the monomer ^{15}N resonances. Most importantly, the saturation profiles are clearly residue specific (Fig. 1b–d, circles). Relatively narrow profiles are observed for residues in the amino(N)-terminal region (Fig. 1b), and very broad profiles for residues in the central (residues 17–21, for example, Fig. 1c) and part of the C-terminal (residues 30–40) hydrophobic regions. Intermediate profiles are observed for residues in the hydrophilic region spanning residues 25–29 (Fig. 1d) as well as for the three C-terminal residues. Qualitatively similar behaviour is observed for the 160-μM Aβ42 sample (Supplementary Fig. 10a–d). The observed residue-specific saturation transfer profiles indicate that, when bound to the surface of the protofibrils, the average ^{15}N-R_2 for each residue is highly sequence-position dependent.

The ^{15}N-DEST profiles can be quantitatively interpreted by incorporating a model of equilibrium chemical exchange within the framework of the McConnell equations[22,23]. The simplest model describing the equilibrium between free monomer ($M_{monomer}$) and peptide transiently bound to the surface of the protofibril ($M_{oligomer}$) is a pseudo-first-order process characterized by global first-order apparent association (k_{on}^{app}) and dissociation (k_{off}) rate constants (Fig. 2a) and residue-specific ^{15}N-R_1 (longitudinal) and R_2 (transverse) values for the free monomer and protofibril-bound states. The value of the k_{on}^{app} can be estimated from the difference, ΔR_2, in ^{15}N-R_2 values between the samples with protofibrils present and the monomeric reference sample (50 μM)[15]. Because transverse magnetization for the protofibril-bound states decays extremely rapidly, the maximum observed ΔR_2 value, ΔR_2^{max}, is equal to k_{on}^{app} under pseudo-equilibrium conditions (note that the observed ΔR_2 values are independent of nucleus and magnetic field[15]; see also Supplementary section 5 for a simple explanation of ΔR_2 and DEST experiments and their interpretation). The saturation profiles at two radio-frequency field strengths (170 and 350 Hz) and the ΔR_2 data for all residues (Fig. 1e for Aβ40 and Supplementary Fig. 10e for Aβ42) were fitted simultaneously, optimizing the values of k_{on}^{app} and k_{off}, and the residue-specific ^{15}N-R_2 values for the protofibril-bound species (see Methods). The ^{15}N-R_1 and R_2 values for the monomer were taken from relaxation data recorded on the low concentration (50 μM) sample. Although the ^{15}N-R_1 values for the protofibril-bound state are unknown, these ^{15}N-R_1 values have no effect on the fitted parameters within their uncertainties over the expected range ($2\,s^{-1} \geq {}^{15}$N-$R_1 \geq 0.01\,s^{-1}$) owing to the design of the experiment (see Methods). The simple two-state model fails to account simultaneously for all the experimental data in the case of both Aβ40 (Fig. 1b–e) and Aβ42 (Supplementary Fig. 10), with systematic deviations for the DEST profiles (Fig. 1b–d, dashed lines) and failure to reproduce ΔR_2 as a function of sequence (Fig. 1e, grey open circles). Extension to a three-site exchange model that adds an intermediate species either on- or off-pathway, introducing additional unknown rate constants connecting monomer, intermediate and protofibril-bound states and residue-specific ^{15}N-R_2 values for the intermediate state, also fails to fit the experimental data.

The above results led us to investigate a simple modification of the two-state model in which the ensemble of protofibril-bound states is divided into two subsets where a given residue is either in direct contact

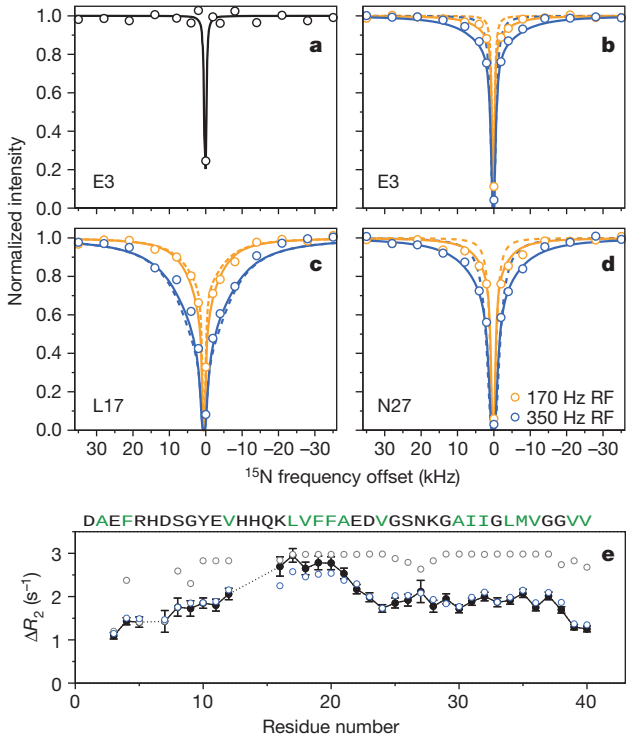

Figure 1 | ^{15}N DEST and ΔR_2 for Aβ40. Examples of normalized cross-peak intensities as a function of frequency offset from the ^{15}N carrier (118.5 p.p.m.): **a**, Glu 3 in the 50 μM Aβ40 sample (radio-frequency field strength of ^{15}N saturation pulse = 170 Hz); **b**, **c** and **d**, Glu 3, Leu 17 and Asn 27, respectively, in the 270 μM Aβ40 sample with ^{15}N saturation at radio-frequency field strengths of 170 (orange circles) and 350 (blue circles) Hz. The solid line in **a** is the calculated saturation profile for a ^{15}N spin with the experimentally determined relaxation rates for monomeric Aβ40. The dashed and solid lines in **b**–**d** are the best-fits to an exchange model with a single protofibril-bound state (cf. Fig. 2a) and to a model incorporating residues tethered and in direct contact with the protofibril (cf. Fig. 2b), respectively. The s.d. of the DEST experimental data points is approximately equal to the size of the circles. **e**, Observed (black filled circles; error bars, 1 s.d.) compared with calculated ΔR_2 values for the first (grey circles) and second (blue circles) models. The reduced χ^2 for the simultaneous best-fit to the DEST and ΔR_2 data are 9.0 for the first model and 1.8 for the second.

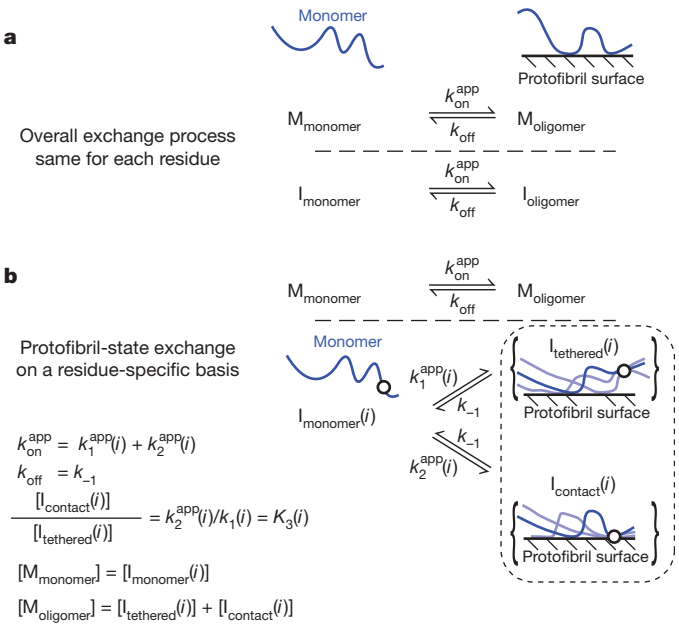

Figure 2 | Kinetic schemes for monomer exchange on the surface of Aβ protofibrils. a, The protofibril-bound peptide ($M_{oligomer}$) exists in only a single state. **b**, The protofibril-bound peptide exists as a large ensemble of states such that each residue can be either tethered or in direct contact with the surface of the oligomer with $K_3(i) = k_2^{app}(i)/k_1^{app}(i)$. The circle in the diagrammatic representation of the states represents a single residue that is either tethered or in direct contact and for which three possible chain configurations are shown.

with the protofibril surface ($I_{contact}$) or tethered ($I_{tethered}$) by residues in direct contact with the protofibril (Fig. 2b). The key to understanding this model lies in the observation that the variations in both ΔR_2 and ^{15}N-DEST profiles are residue specific. This variation cannot be accounted for by postulating the existence of low molecular mass oligomers because, in that case, the ΔR_2 and DEST effects would be uniform throughout the peptide sequence (as each residue would be subject to the same events and the same average relaxation behaviour when bound to the surface of the oligomers). Thus for each residue, i, there is a potentially different partitioning of the large number of conformational states into $I_{tethered}(i)$ and $I_{contact}(i)$. This partitioning is computed for a single residue at a time, the state of the other residues may be tethered, bound or inter-converting between the two, and the correlation between states at different positions is not considered. Critical to the simplicity of the model is the retention of the overall two-state association/dissociation process; the global apparent association rate constant for the conversion of monomer to the protofibril-bound ensemble, k_{on}^{app}, is given by the sum of the pseudo-first-order rate constants $k_1^{app}(i)$ and $k_2^{app}(i)$ for the conversion of a residue i from the monomeric state ($I_{monomer}$) to $I_{tethered}(i)$ and $I_{contact}(i)$, respectively; the global dissociation rate constant, k_{off}, from protofibril-bound states to monomer, is the same for $I_{tethered}(i)$ and $I_{contact}(i)$ for all residues i (that is, $k_{off} = k_{-1} = k_{-2}$). Thus, the two-state equilibrium between monomer and protofibril-bound forms is preserved, and k_{on}^{app} and k_{off} represent ensemble averaged rates. This model adds the fewest parameters to describe a system with a huge number of potential configurations (2^{40} and 2^{42} for Aβ40 and Aβ42, respectively, where each residue is represented as either tethered or in direct contact) with differing behaviour at each residue. Because there are so many combinations of states, the addition of further variation from the polydispersity of the protofibrils does not impact the interpretation of the data or its quantitative analysis in terms of the model in Fig. 2b.

A residue-specific equilibrium between the tethered and direct-contact states is described by the ratio of $I_{contact}(i)$ to $I_{tethered}(i)$, $K_3(i) = k_2^{app}(i)/k_1^{app}(i)$. Direct inter-conversion between $I_{contact}(i)$ and $I_{tethered}(i)$ is not necessary to fit the data and, hence, is not incorporated in the analysis presented in the main text (see Supplementary Table 1 and Supplementary Fig. 11 for analysis including these kinetic paths). The ^{15}N$-R_2^{tethered}$ values for the $I_{tethered}$ states are also residue-specific and describe the average dynamics of a given residue in the tethered state. In physical terms, this will depend upon the average length and flexibility of the segment separating residue i from other residues of the peptide in direct contact with the oligomer.

The model in Fig. 2b is a reduced, 'model-free' representation of the actual system, which clearly comprises a large ensemble of different states and inter-conversion networks. Although the model is phenomenological in that individual protofibril-bound states in the ensemble and the correlated behaviour of residues are not explicitly considered, the smooth variation of the fitted parameters as a function of residue is indicative of correlated behaviour at adjacent positions, as to be expected for a model that well describes physical behaviour. Further, the model does not require that a single protofibril state be present or that the members of the protofibril ensemble even have the same interfaces with bound monomers. The ability to interpret the experimentally observed residue-by-residue differences between Aβ40 and Aβ42 demonstrates the success of the model.

Least-squares nonlinear optimization of the scheme shown in Fig. 2b results in excellent fits to both the ^{15}N-DEST saturation profiles (Fig. 1b–d and Supplementary Fig. 10a–d) and the ΔR_2 data (Fig. 1e and Supplementary Fig. 10e). For Aβ40 at 270 μM, $k_{on}^{app} = 3.0 \pm 0.7\ s^{-1}$, in agreement with the observed value of $3.0\ s^{-1}$ for ΔR_2^{max} (Fig. 1e), and $k_{off} = 51 \pm 12\ s^{-1}$, in good agreement with our previous estimate of approximately $73\ s^{-1}$ obtained from a one-dimensional ^{1}H saturation experiment[15]. The values of k_{on}^{app} and k_{off} for Aβ42 at 160 μM are $2.4\ s^{-1}$ (in agreement with $2.3\ s^{-1}$ for ΔR_2^{max}) and $62\ s^{-1}$, respectively, although the standard deviations in these fitted parameters are higher owing to lower experimental signal-to-noise ($\pm 1.8\ s^{-1}$ and $\pm 46\ s^{-1}$). The values of ^{15}N$-R_2^{contact}$ are $18{,}800 \pm 700\ s^{-1}$ and $19{,}300 \pm 2000\ s^{-1}$ for Aβ40 and Aβ42, respectively, which are reasonable for the large, worm-like protofibrils seen in these samples by atomic force and electron microscopy (Supplementary Fig. 1). From the values of the association and disassociation rate constants one can deduce that the populations of transiently bound Aβ40 and Aβ42 are approximately 6% and 4%, respectively, that of free monomer.

The residue-specific partitioning, $K_3(i)$, between the direct-contact and tethered states (Fig. 3a) and the associated ^{15}N$-R_2^{tethered}$ relaxation values (Fig. 3b) provide the first characterization of the protofibril-bound forms of Aβ40 and Aβ42 at the single-residue level. Qualitatively the K_3 and ^{15}N$-R_2^{tethered}$ profiles for Aβ40 and Aβ42 are similar, with the notable exception of the ^{15}N$-R_2^{tethered}$ values for the C-terminal residues. We also note that the values of K_3 and ^{15}N$-R_2^{tethered}$ are directly correlated with the observed widths of the saturation profiles and ΔR_2, respectively (Supplementary Fig. 12), demonstrating that the model is consistent with a qualitative analysis of the data suggested directly from the observed residue-specific behaviour.

For both Aβ40 and Aβ42 the first eight N-terminal residues have similar, small values of K_3 (0.08–0.14), indicating that these residues are predominantly tethered, spending only a small fraction (≤10%) of the time in actual direct contact with the protofibril surface. Correlated with this finding, these residues retain considerable flexibility as reflected by ^{15}N$-R_2^{tethered}$ values ranging from 20 to $80\ s^{-1}$. These observations are consistent with ^{13}C linewidths in solid-state NMR spectra of Aβ40 fibrils that are indicative of conformational disorder for the N-terminal segment[10], although our data indicate a small but measurable population in direct contact with the protofibril surface.

The highest values of K_3 (>0.24) are seen for residues 16–25 and 28–37 of Aβ40 and residues 16–23 and 33–40 of Aβ42, corresponding roughly to the central and C-terminal hydrophobic regions that form intermolecular β-sheets at the core of amyloid fibrils[9,10]. Although the ratio of direct-contact to tethered states in the Aβ40 protofibril-bound ensemble is very similar for the two regions (0.34 ± 0.06 compared with 0.32 ± 0.04), the average ^{15}N$-R_2^{tethered}$ values are very different: $146 \pm 33\ s^{-1}$ for residues 16–22 falling to $61 \pm 16\ s^{-1}$ for residues 23–25, and $62 \pm 13\ s^{-1}$ for residues 28–37. This suggests that, in the tethered states, residues 28–37 of Aβ40 are considerably more flexible than residues 16–22. In terms of a physical picture this suggests that

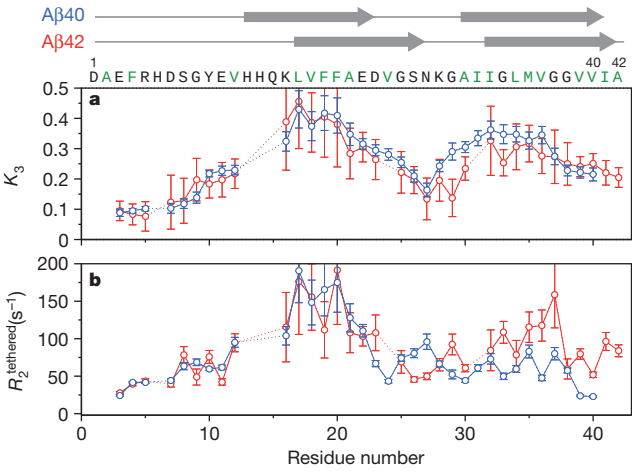

Figure 3 | Comparison of residue-specific fitted parameters describing the ensemble of protofibril-bound states. **a**, Residue-specific equilibrium constant (K_3) for the relative partitioning of direct-contact and tethered states on the surface of the protofibrils. **b**, ^{15}N$-R_2^{tethered}$ values for the tethered states. The values for Aβ40 and Aβ42 are displayed as blue and red circles, respectively. The proposed two β-strand regions in fibrils of Aβ40 and Aβ42 (refs 9 and 8, respectively) are indicated by arrows at the top of the figure. Error bars, 1 s.d.

the C-terminal region of Aβ40 may be far from the protofibril surface when other residues (such as the 16–22 region) are bound, whereas the converse is true for the 16–22 region. For Aβ42, the average value of K_3 is slightly higher in the central hydrophobic region (0.35 ± 0.06) compared with the 33–40 region (0.28 ± 0.03), but in contrast to Aβ40, the corresponding $^{15}N-R_2^{tethered}$ average values are quite similar ($133 \pm 33\ s^{-1}$ and $99 \pm 35\ s^{-1}$, respectively), suggesting that the tethered states of the C-terminal hydrophobic region are on average less mobile and closer to the protofibril surface in Aβ42 than in Aβ40.

The most striking differences between protofibril-bound Aβ40 and Aβ42 are seen at the C terminus. Intermediate K_3 values (0.21–0.23) associated with low $^{15}N-R_2^{tethered}$ values (58, 24 and 23 s^{-1} for residues 38, 39 and 40, respectively) are observed for the last three C-terminal residues of Aβ40 (Fig. 3). Thus, residues 38–40 in the ensemble of Aβ40 protofibril-bound states are more mobile and hence significantly less often buried than the central (residues 16–25) and C-terminal (residues 28–37) hydrophobic regions. This is in sharp contrast to Aβ40 fibrils, where the C-terminal residues are located at the central core of the fibre, forming tight intermolecular contacts with both neighbouring strands in the C-terminal cross-β sheet and adjacent subunits in the supramolecular structure[9]. Interestingly, the last two C-terminal residues of antibody-stabilized Aβ40 protofibrils also exhibit increased mobility as assessed by solid state NMR[19], suggesting that enhanced dynamics of the C-terminal residues of Aβ40 are at least partly conserved when the protofibril-bound states are incorporated into the protofibril core. Although the population of direct-contact states for the C-terminal residues of Aβ42 is similar to that of Aβ40 (Fig. 3a), the corresponding $^{15}N-R_2^{tethered}$ values are significantly higher for Aβ42 ($76 \pm 16\ s^{-1}$ for residues 39–42 of Aβ42 compared with $23.5 \pm 0.5\ s^{-1}$ for residues 39–40 of Aβ40; Fig. 3b). Thus, the mobility of the C-terminal residues in the tethered states of Aβ42 is hindered relative to that in Aβ40.

If dynamics of the C-terminal hydrophobic region and C-terminal residues in the protofibril-bound states, where Aβ40 and Aβ42 differ (Fig. 3), constitute the apparent free-energy barrier in the nucleation-dependent conformational change or polymerization separating disordered oligomers from fast-elongating amyloid fibrils[24], these observed differences may explain the higher rate of protofibril and fibril formation of Aβ42 relative to Aβ40 (refs 13, 14).

Further, although the population of direct-contact states for the hydrophilic region between residues 27 and 29 is reduced for both Aβ40 and Aβ42, the K_3 values are higher for Aβ40 than Aβ42 (Fig. 3a). Because this region constitutes a hairpin turn in Aβ fibrils, the lower population of direct contact states for Aβ42 may facilitate hairpin and subsequent β-sheet formation, thereby enhancing the rate of incorporation of surface-bound monomers into the protofibril core.

In summary, ^{15}N-DEST and ΔR_2 measurements probe exchange processes between monomer and protofibril-bound states of Aβ on times scale of 10–100 ms, and imprint the residue-by-residue footprint of the 'dark' protofibril-bound state on the easily observed monomer. These experiments are complementary to pulsed H/D exchange experiments that have been used to probe fibril formation and recycling on a million-fold slower timescale[25,26], as well as to spin-state selective methyl group relaxation dispersion experiments[27] that probe invisible state dynamics of supramolecular complexes on the intermediate chemical shift timescale of 50 μs to 10 ms (ref. 28). In contrast to relaxation dispersion, which requires that the visible and invisible states have different chemical shifts, the DEST and ΔR_2 experiments rely entirely on large differences in transverse relaxation rates (R_2). For systems where a relatively small particle (that is, a macromolecule whose resonances are directly observable by solution NMR) is in exchange with a state bound to a large particle (for example, an aggregate, a fibril, a large supramolecular complex or a solid support), large differences in R_2 values will be present and consequently the R_2 values in the 'dark' state can be determined by DEST. The DEST experiment requires only that the exchange rate ($k_{on}^{app} + k_{off}$) be larger than the ^{15}N-R_1 of the observed species. The Aβ monomer has a ^{15}N-R_1 of approximately $1.5\ s^{-1}$, significantly faster and hence more limiting than for a larger protein. Because k_{on}^{app} is a pseudo-first-order rate constant, the use of higher concentrations can increase the apparent on-rate, thereby extending the range of applicability. The upper limit on the value of k_{on}^{app} is approximately $100\ s^{-1}$, beyond which accurate determination of ΔR_2 is difficult. We anticipate that the DEST technique for examining dynamics at single-residue resolution of otherwise invisible 'dark' states will be applicable to many areas of current interest both in biology (for example, the interaction of unfolded proteins with the proteasome[29] and very large chaperones, the formation of low-affinity, large supramolecular complexes, and the folding-upon-binding[30] of intrinsically disordered proteins) and materials science (for example, exchange reactions on surfaces).

METHODS SUMMARY

Solutions of uniformly ^{15}N-labelled Aβ40 and Aβ42 were prepared from NaOH-treated stocks as described previously[15]. NMR samples, comprising 50 and 270 μM Aβ40 and 50 and 160 μM Aβ42 in 50 mM HEPES, pH 6.8, and 90% H_2O/10% D_2O, were prepared and maintained at 4–10 °C at all times. All NMR experiments were conducted at 10 °C on a Bruker 900 MHz spectrometer equipped with a triple resonance z-gradient cryoprobe. Fitting the DEST and ΔR_2 data to various kinetic schemes using the McConnell equations to determine the oligomer-bound R_2 values and kinetic parameters was performed as described in Methods.

Full Methods and any associated references are available in the online version of the paper at www.nature.com/nature.

Received 19 June; accepted 19 September 2011.
Published online 30 October 2011.

1. Lashuel, H. A. & Lansbury, P. T. Are amyloid diseases caused by protein aggregates that mimic bacterial pore-forming toxins? *Q. Rev. Biophys.* **39,** 167–201 (2006).
2. Walsh, D. M. & Selkoe, D. J. Aβ oligomers – a decade of discovery. *J. Neurochem.* **101,** 1172–1184 (2007).
3. Glabe, C. G. Structural classification of toxic amyloid oligomers. *J. Biol. Chem.* **283,** 29639–29643 (2008).
4. Querfurth, H. W. & LaFerla, F. M. Mechanisms of disease: Alzheimer's disease. *N. Engl. J. Med.* **362,** 329–344 (2010).
5. Ahmed, M. *et al.* Structural conversion of neurotoxic amyloid-β_{1-42} oligomers to fibrils. *Nature Struct. Mol. Biol.* **17,** 561–567 (2010).
6. Fukumoto, H. *et al.* High-molecular-weight beta-amyloid oligomers are elevated in cerebrospinal fluid of Alzheimer patients. *FASEB J.* **24,** 2716–2726 (2010).
7. Petkova, A. T. *et al.* A structural model for Alzheimer's β-amyloid fibrils based on experimental constraints from solid state NMR. *Proc. Natl Acad. Sci. USA* **99,** 16742–16747 (2002).
8. Luhrs, T. *et al.* 3D structure of Alzheimer's amyloid-β(1–42) fibrils. *Proc. Natl Acad. Sci. USA* **102,** 17342–17347 (2005).
9. Paravastu, A. K., Leapman, R. D., Yau, W. M. & Tycko, R. Molecular structural basis for polymorphism in Alzheimer's β-amyloid fibrils. *Proc. Natl Acad. Sci. USA* **105,** 18349–18354 (2008).
10. Petkova, A. T., Yau, W. M. & Tycko, R. Experimental constraints on quaternary structure in Alzheimer's β-amyloid fibrils. *Biochemistry* **45,** 498–512 (2006).
11. Fawzi, N. L., Okabe, Y., Yap, E. H. & Head-Gordon, T. Determining the critical nucleus and mechanism of fibril elongation of the Alzheimer's $A\beta_{1-40}$ peptide. *J. Mol. Biol.* **365,** 535–550 (2007).
12. Powers, E. T. & Powers, D. L. Mechanisms of protein fibril formation: nucleated polymerization with competing off-pathway aggregation. *Biophys. J.* **94,** 379–391 (2008).
13. Jarrett, J. T., Berger, E. P. & Lansbury, P. T. Jr. The carboxy terminus of the beta amyloid protein is critical for the seeding of amyloid formation: implications for the pathogenesis of Alzheimer's disease. *Biochemistry* **32,** 4693–4697 (1993).
14. Riek, R., Guntert, P., Dobeli, H., Wipf, B. & Wuthrich, K. NMR studies in aqueous solution fail to identify significant conformational differences between the monomeric forms of two Alzheimer peptides with widely different plaque-competence, Aβ(1–40)(ox) and Aβ(1–42)(ox). *Eur. J. Biochem.* **268,** 5930–5936 (2001).
15. Fawzi, N. L., Ying, J., Torchia, D. A. & Clore, G. M. Kinetics of amyloid β monomer-to-oligomer exchange by NMR relaxation. *J. Am. Chem. Soc.* **132,** 9948–9951 (2010).
16. Teplow, D. B. *et al.* Elucidating amyloid β-protein folding and assembly: a multidisciplinary approach. *Acc. Chem. Res.* **39,** 635–645 (2006).
17. Mastrangelo, I. A. *et al.* High-resolution atomic force microscopy of soluble Aβ42 oligomers. *J. Mol. Biol.* **358,** 106–119 (2006).
18. Pimplikar, S. W. Reassessing the amyloid cascade hypothesis of Alzheimer's disease. *Int. J. Biochem. Cell Biol.* **41,** 1261–1268 (2009).
19. Scheidt, H. A., Morgado, I., Rothemund, S., Huster, D. & Fandrich, M. Solid-state NMR spectroscopic investigation of Aβ protofibrils: implication of a β-sheet remodeling upon maturation into terminal amyloid fibrils. *Angew. Chem.* **50,** 2837–2840 (2011).

20. Hou, L. M. *et al.* Solution NMR studies of the Aβ(1–40) and Aβ(1–42) peptides establish that the met35 oxidation state affects the mechanism of amyloid formation. *J. Am. Chem. Soc.* **126,** 1992–2005 (2004).
21. Yan, Y. & Wang, C. Aβ42 is more rigid than Aβ40 at the C terminus: implications for Aβ aggregation and toxicity. *J. Mol. Biol.* **364,** 853–862 (2006).
22. McConnell, H. M. Reaction rates by nuclear magnetic resonance. *J. Chem. Phys.* **28,** 430–431 (1958).
23. Helgstrand, M., Hard, T. & Allard, P. Simulations of NMR pulse sequences during equilibrium and non-equilibrium chemical exchange. *J. Biomol. NMR* **18,** 49–63 (2000).
24. Lee, J., Culyba, E. K., Powers, E. T. & Kelly, J. W. Amyloid-β forms fibrils by nucleated conformational conversion of oligomers. *Nature Chem. Biol.* **7,** 602–609 (2011).
25. Carulla, N. *et al.* Molecular recycling within amyloid fibrils. *Nature* **436,** 554–558 (2005).
26. Carulla, N., Zhou, M., Giralt, E., Robinson, C. V. & Dobson, C. M. Structure and intermolecular dynamics of aggregates populated during amyloid fibril formation studied by hydrogen/deuterium exchange. *Acc. Chem. Res.* **43,** 1072–1079 (2010).
27. Hansen, D. F., Vallurupalli, P. & Kay, L. E. Measurement of methyl group motional parameters of invisible, excited protein states by NMR spectroscopy. *J. Am. Chem. Soc.* **131,** 12745–12754 (2009).
28. Ishima, R. & Torchia, D. A. Accuracy of optimized chemical-exchange parameters derived by fitting CPMG R_2 dispersion profiles when $R_2^{0a} \neq R_2^{0b}$. *J. Biomol. NMR* **34,** 209–219 (2006).
29. Ruschak, A. M., Religa, T. L., Breuer, S., Witt, S. & Kay, L. E. The proteasome antechamber maintains substrates in an unfolded state. *Nature* **467,** 868–871 (2010).
30. Sugase, K., Dyson, H. J. & Wright, P. E. Mechanism of coupled folding and binding of an intrinsically disordered protein. *Nature* **447,** 1021–1025 (2007).

Supplementary Information is linked to the online version of the paper at www.nature.com/nature.

Acknowledgements We thank R. Tycko for discussions, D. Baber, D. Garrett and M. Cai for NMR technical assistance, F. Shewmaker for performing dot blots, and W. Qiang, B. Chen and K. Thurber for assistance with atomic force microscopy and electron microscopy imaging. This work was supported by the intramural program of the National Institute of Diabetes and Digestive and Kidney Diseases/National Institutes of Health and the AIDS Targeted Antiviral Program of the Office of the Director of the National Institutes of Health (to G.M.C.).

Author Contributions All authors contributed extensively to the work described in this paper.

Author Information Reprints and permissions information is available at www.nature.com/reprints. The authors declare no competing financial interests. Readers are welcome to comment on the online version of this article at www.nature.com/nature. Correspondence and requests for materials should be addressed to G.M.C. (mariusc@mail.nih.gov).

METHODS

Description of the two-dimensional ^{15}N-DEST experiment and pulse sequence. Owing to relatively small equilibrium magnetization of ^{15}N nuclei, initial amide hydrogen ($^{1}H_N$) magnetization for the monomeric species is transferred to longitudinal ^{15}N magnetization, after which a weak ^{15}N saturation pulse is applied at a series of radio-frequency offsets (ranging from +35 to −35 kHz) for a sufficient length of time (0.9 s) to allow the monomeric peptide to sample a protofibril-bound state where ^{15}N-R_2 values are orders of magnitude larger than in the monomeric species and allow for efficient partial saturation by the weak radio-frequency field. Partial saturation is then transferred back to the monomeric state by chemical exchange, and recorded as a decrease in intensity of the ^{1}H–^{15}N correlation cross-peaks for the NMR observable monomeric species relative to that in a reference spectrum obtained without saturation (see Supplementary Fig. 8). Because initial $^{1}H_N$ to ^{15}N INEPT transfer of magnetization in the high molecular mass protofibrils is extremely inefficient owing to very fast ^{1}H and ^{15}N transverse relaxation, the observed transfer-of-saturation only arises from peptides that begin the experiment as monomers, are incorporated into protofibrils, and subsequently released within the saturation time. The pulse sequence for the two-dimensional heteronuclear single quantum coherence correlation-based ^{15}N-DEST experiment is shown in Supplementary Fig. 8. The pulse sequence is similar in spirit to that commonly used for measuring ^{15}N-R_1 longitudinal relaxation except that the variable T_1 relaxation delay is replaced by a weak, continuous-wave saturation pulse at variable radio-frequency offsets. The DEST experiment begins from the amide proton magnetization H_z of the monomeric peptide. Following the first INEPT transfer, longitudinal two spin order $2H_zN_z$ is obtained (Supplementary Fig. 8, point *a*). The subsequent refocusing INEPT provides in phase N_z magnetization (Supplementary Fig. 8, point *b*). The 90° ^{1}H pulse ϕ_2 not only flips the water signal back to the +*z*-axis, but also purges any residual anti-phase magnetization $2N_yH_z$ before the ^{15}N continuous-wave saturation pulse. The latter is applied for 0.9 s at a series of 15 different offsets (35, 28, 21, 14, 8, 4, 2, 0, −2, −4, −8, −14, −21, −28 and −35 kHz) from the ^{15}N carrier frequency (set to 118.5 and 117.6 p.p.m. and located at the centre of the monomer spectrum of Aβ40 and Aβ42, respectively) and at two radio-frequency field strengths (170 and 350 Hz). In addition, two reference spectra were recorded at each concentration without saturation. During the continuous-wave ^{15}N pulse, the magnetization (N_z) originating from the monomeric peptide is partly saturated when the peptide samples a protofibril-bound state. The latter cannot be directly observed owing to extremely rapid transverse (R_2) relaxation. This partial saturation results in a reduction of the N_z magnetization by a multiplicative factor κ (relative to that in the reference spectrum with the saturation pulse turned off) which depends on the strength and frequency of the ^{15}N saturation pulse as well as on the kinetics of the monomer-oligomer exchange process (see main text for more details), thereby providing valuable insight into the inter-conversion dynamics at atomic resolution. When the oligomer-bound peptide is released back into solution as a monomer, its reduced magnetization κN_z is detected by heteronuclear single quantum correlation. It is important to note that inversion of the phases of both the 90° ^{1}H pulse ϕ_1 and the receiver phase alternates the orientation of the N_z magnetization between the +*z* and –*z*-axes. Summation of transients with these alternating phases removes non-exponential contributions to longitudinal relaxation (for example, owing to non-zero magnetization at Boltzman equilibrium) so that loss of magnetization due to R_1 relaxation at the end of the continuous-wave saturation pulse is a simple scaling factor $e^{-R_1 t}$, and hence the R_1 dependence is effectively removed when cross-peak intensities are normalized to those in the spectrum without saturation[31]. Longitudinal cross-correlated relaxation interference between the ^{15}N–^{1}H dipolar interaction and the ^{15}N chemical shift anisotropy is eliminated by application of the 180° ^{1}H pulse train (with an inter-pulse delay of 100 ms) during the continuous-wave ^{15}N pulse. With a cryogenic probe at a ^{1}H spectrometer frequency of 900 MHz, this inter-pulse delay is sufficient to return the water signal back to the +*z*-axis through radiation damping. The de-phasing INEPT following the saturation period results in an anti-phase term $\kappa 2N_xH_z$ (Supplementary Fig. 8, point *c*). The anti-phase ^{15}N magnetization is then converted to amide proton anti-phase magnetization. The last refocusing INEPT, incorporating a WATERGATE scheme, not only re-phases the anti-phase proton magnetization to in-phase κH_x, but also suppresses the residual water signal before direct detection of the monomeric peptide amide proton magnetization.

Data acquisition and analysis. Solutions of uniformly ^{15}N-labelled Aβ40 and Aβ42 were prepared from NaOH-treated stocks as described previously[15]. NMR samples, comprising 50 and 270 μM Aβ40 and 50 and 160 μM Aβ42 in 50 mM HEPES, pH 6.8, and 90% H_2O/10% D_2O, were prepared and maintained at 4–10 °C at all times. All NMR experiments were recorded at 10 °C using a Bruker Avance-III spectrometer operating at ^{1}H frequency 900.27 MHz and equipped with a Bruker TCI *z*-axis gradient cryogenic probe. ^{15}N-R_2 data on the 50 and 270 μM Aβ40 samples and 50 and 160 μM Aβ42 samples and ^{15}N-R_1 data at 50 μM were measured using standard interleaved two-dimensional ^{1}H–^{15}N heteronuclear single quantum coherence correlation-based NMR experiments and analysed as described previously[15].

The two-dimensional ^{15}N-DEST spectra were acquired as 32 interleaved experiments (with the radio-frequency field strengths and frequencies for the continuous-wave ^{15}N pulse given above). For Aβ40, each two-dimensional experiment comprises 154* × 1,900* complex data points in the indirect ^{15}N and direct ^{1}H dimensions, respectively, with corresponding acquisition time of 77 and 175.6 ms. For Aβ42, 78* × 1,900* complex points were acquired with acquisition times of 41 and 175.6 ms. Sixteen transients for Aβ40 and 32 for Aβ42 were collected per free induction decay with a 1.7-s delay between scans. The total experimental times for Aβ40 and Aβ42 were each approximately 5 days.

The complete interleaved two-dimensional data set was first split into 32 individual two-dimensional data sets, one for each experiment at a particular ^{15}N saturation pulse power level and frequency, using a C program written in-house. Each experiment was then processed identically and analysed using NMRPipe[32]. The time-domain data in each spectrum were apodized in the indirect ^{15}N dimension with a 54°-shifted sine bell function. For the direct ^{1}H dimension, an exponential window function with a line broadening of 5 Hz for Aβ40 and 8 Hz for Aβ42 was applied, followed in the case of the Aβ40 data by a 72°-shifted squared sine bell. The additional line-broadening for the Aβ42 data was used to improve the signal-to-noise owing to the very low (approximately 35 μM) concentration of free Aβ42 monomer. Time-domain data in the ^{15}N and ^{1}H dimensions were then zero-filled to obtain a final complex 1024* × 4096* data matrix, with digital resolutions of 2.0 and 2.6 Hz, respectively. The residue-specific signal reduction factor κ as a function of frequency offset of the continuous-wave ^{15}N saturation pulse was obtained from the ratio of peak heights in the saturation experiment versus the reference experiment with the saturation pulse turned off. (The Bruker pulse sequence and acquisition parameter files for the ^{15}N-DEST experiment, as well as the processing scripts, are available on request.)

Simultaneous fitting of the DEST and ΔR_2 data to kinetic models. A homogenous form of the McConnell equations[22] describing a single spin in chemical exchange, as presented in equation (21) of ref. 23, was expanded to a three-state system. Owing to the small gyromagnetic ratio of ^{15}N nuclei and their sparse density in proteins, cross-relaxation between neighbouring ^{15}N nuclei in both monomer and protofibril-bound states is negligible, in marked contrast with the one-dimensional ^{1}H transfer-of-saturation profiles reported previously[15]. Effects on the saturation owing to cross-relaxation between ^{15}N and directly bonded ^{1}H nuclei, though predicted to be small, are removed with phase-cycling, placing the initial ^{15}N magnetization during the saturation period on the +*z* and –*z*-axes in alternating transients and measuring their intensity difference. The time dependence of the magnetization is given by:

$$\frac{d}{dt}\begin{bmatrix} E/2 \\ I_x^A \\ I_y^A \\ I_z^A \\ I_x^B \\ I_y^B \\ I_z^B \\ I_x^C \\ I_y^C \\ I_z^C \end{bmatrix} = \begin{bmatrix} 0 & 0 & 0 & 0 & 0 & 0 & 0 & 0 & 0 & 0 \\ 0 & \lambda^A+k_1+k_2 & \Omega^A & -\omega_y & -k_{-1} & 0 & 0 & -k_{-2} & 0 & 0 \\ 0 & -\Omega^A & \lambda^A+k_1+k_2 & \omega_x & 0 & -k_{-1} & 0 & 0 & -k_{-2} & 0 \\ -2\Theta^A & \omega_y & -\omega_x & \rho^A+k_1+k_2 & 0 & 0 & -k_{-1} & 0 & 0 & -k_{-2} \\ 0 & -k_1 & 0 & 0 & \lambda^B+k_{-1}+k_3 & \Omega^B & -\omega_y & -k_{-3} & 0 & 0 \\ 0 & 0 & -k_1 & 0 & -\Omega^B & \lambda^B+k_{-1}+k_3 & \omega_x & 0 & -k_{-3} & 0 \\ -2\Theta^B & 0 & 0 & -k_1 & \omega_y & -\omega_x & \rho^B+k_{-1}+k_3 & 0 & 0 & -k_{-3} \\ 0 & -k_2 & 0 & 0 & -k_3 & 0 & 0 & \lambda^C+k_{-2}+k_{-3} & \Omega^C & -\omega_y \\ 0 & 0 & -k_2 & 0 & 0 & -k_3 & 0 & -\Omega^C & \lambda^C+k_{-2}+k_{-3} & \omega_x \\ -2\Theta^C & 0 & 0 & -k_2 & 0 & 0 & -k_3 & \omega_y & -\omega_x & \rho^C+k_{-2}+k_{-3} \end{bmatrix} \times \begin{bmatrix} E/2 \\ I_x^A \\ I_y^A \\ I_z^A \\ I_x^B \\ I_y^B \\ I_z^B \\ I_x^C \\ I_y^C \\ I_z^C \end{bmatrix} \quad (1)$$

where *I* represents the magnetizations of the ^{15}N spins in the rotating frame in the free monomer, and in the tethered and direct-contact protofibril-bound states (denoted by the superscripts *A*, *B* and *C*, respectively). The relaxation rates for transverse and longitudinal magnetization are λ and ρ, respectively; Ω is the resonance offset frequency calculated as the difference between the peak resonance frequency (accounting for peak folding in the case of Aβ42 Ala 42) and

the ^{15}N carrier frequency + continuous-wave pulse offset, and ω the radio-frequency field strength of the continuous-wave saturation pulse applied along the appropriate axis; E is unity; and Θ is related to the equilibrium magnetization as described by Helgstrand *et al.*[23]. The rate constants are as follows (see Fig. 2b): k_1 and k_2 are the apparent first-order rate constants for the forward reaction from the monomer to the tethered and direct-contact protofibril-bound states, respectively; k_{-1} and k_{-2} are the corresponding dissociation rate constants and in this instance $k_{-1} = k_{-2}$ (see main text); k_3 and k_{-3} (not shown in Fig. 2b) are the rate constants for the conversion of tethered to direct-contact states, and vice versa, respectively. Detailed balance is ensured from the relationship $k_{-3} = k_3k_1/k_2$ (with $k_{-1} = k_{-2}$). The numerical solution for I_z^A, the experimentally observed magnetization in the DEST experiment, after a given saturation time as a function of frequency offset was calculated using the matrix exponential function in the program Matlab. The solution is calculated for both initial ^{15}N magnetization during the saturation period on the $+z$ and $-z$-axes, I_{+z} and I_{-z}, and the difference, $I_{+z} - I_{-z}$, is then computed at each frequency offset and radio-frequency field strength, normalized to the solution without saturation, and compared to the normalized experimentally observed intensity.

ΔR_2 values, for a given set of kinetic and relaxation rate constants, were calculated by subtracting the monomer ^{15}N-R_2 values for each residue, measured experimentally on the monomeric 50 μM samples, from the calculated R_2 values. The calculated R_2 value for a system in equilibrium exchange is computed assuming a single exponential decay:

$$R_2^{\mathrm{calc}} = -\ln\left(\frac{I_x^A(\tau)}{I_x^A(0)}\right)/\tau \qquad (2)$$

where the transverse magnetization, I_x^A, is computed at time $\tau = 0.2$ s and time 0. The choice of 0.2 s for τ was to match to one of the longer delays used in the experimental ^{15}N-R_2 measurements. Simulated delays longer than approximately 20 ms result in the same value of R_2^{calc}, validating the assumption of single exponential decay.

^{15}N relaxation rates in the protofibril-bound states, and kinetic rate constants connecting monomer and protofibril-bound states in all schemes (cf. Fig. 2), were fitted by simultaneous nonlinear least squares minimization of the differences between the observed and calculated (equation (1)) DEST profiles (at both applied radio-frequency field strengths for the continuous-wave ^{15}N saturation pulse) and between the observed and calculated (equation (2)) ΔR_2 values.

31. Sklenar, V., Torchia, D. & Bax, A. Measurement of ^{13}C longitudinal relaxation using ^{1}H detection. *J. Magn. Reson.* **73,** 375–379 (1987).
32. Delaglio, F. *et al.* NmrPipe – a multidimensional spectral processing system based on Unix pipes. *J. Biomol. NMR* **6,** 277–293 (1995).